

Chapter 6

Overview of MinXSS Solar CubeSat

The Miniature X-ray Solar Spectrometer (MinXSS) is a three-unit (3U) CubeSat developed at the Laboratory for Atmospheric and Space Physics at the University of Colorado, Boulder. Over 40 students contributed to the project with professional mentorship and technical contributions from professors in the Aerospace Engineering Sciences Department at University of Colorado, Boulder and from Laboratory for Atmospheric and Space Physics scientists and engineers. I have personally spent over 4500 hours working on MinXSS at the time of this writing. The scientific objective of MinXSS is to study processes in the dynamic sun, from quiet sun to solar flares, and to further understand how these changes in the sun influence the Earths atmosphere by providing unique spectral measurements of solar soft x rays (SXRs). The study of solar eruptive events such as solar flares is the thread tying this chapter and the next together with preceding chapters.

The enabling technology providing the advanced solar SXR spectral measurements is the Amptek X123, a commercial off-the-shelf silicon drift detector. The Amptek X123 has a low mass (324 g after modification), modest power consumption (2.50 W), and small volume (6.86 x 9.91 x 2.54 cm), making it ideal for a CubeSat. This chapter provides an overview of the MinXSS mission: the science objectives, subsystems, and lessons learned.

6.1 Brief CubeSat Introduction

CubeSats are now becoming a viable vehicle for scientific measurements in space. As commercial entities, government laboratories, and universities continue to miniaturize the requisite

technologies for satellites, the sophistication and size of space-based scientific instruments increases. The University of Colorado, Boulder (CU) and the Laboratory for Atmospheric and Space Physics (LASP), developed the Colorado Student Space Weather Experiment (CSSWE; Li et al. 2012; Gerhardt et al. 2013) three-unit (3U) CubeSat, which launched in 2012 and operated for approximately two years. The science instrument measured high-energy electrons and protons in low Earth orbit (LEO) and has resulted in many peer-reviewed journal articles. The present work builds on this success and takes advantage of new commercially available precision three-axis attitude determination and control to achieve fine target pointing toward the sun. To date, the majority of CubeSats have been technology demonstrations; their goal is to increase the technology readiness level of new technologies and old technologies that have been miniaturized for use in CubeSats. MinXSS (shown in Figure 6.1) is a CubeSat with science as its primary mission. So this chapter starts with science.

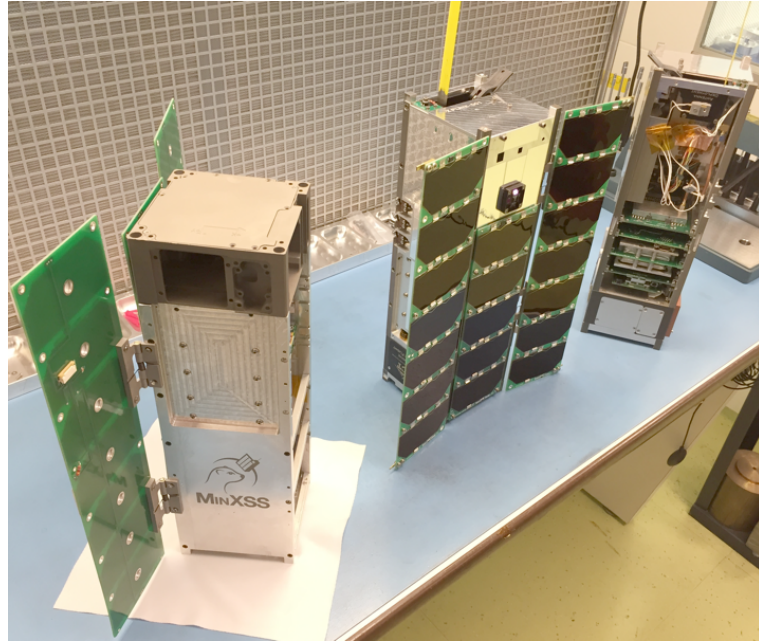


Figure 6.1: Photo of MinXSS family (left to right): prototype unit, flight model (FM)-1, FM-2.

6.2 Science Objectives

There is a rich history of solar SXR spectral observations over the past three decades, but with a significant gap of spectrally resolved measurements in the 0.46 nm range (see Figure 6.2). There were many new discoveries about solar flares during the 1980s using solar SXR spectral measurements from the Department of Defense P78-1, NASA Solar Maximum Mission (SMM), and Japan Aerospace Exploration Agency Hinotori satellites. For example, Doschek (1990) provides results about flare temperatures, electron densities, and elemental abundances for some flares during these missions. A review of flare observations from Yohkoh and the Compton Gamma Ray Observatory (CGRO), for the hard (higher energy) x-ray (HXR) range, is provided in Sterling and Hudson (1997). These earlier missions laid a solid foundation for studies of flare physics and flare spectral variability that the Reuven Ramaty High-Energy Solar Spectroscopic Imager (RHESSI; Lin et al. 2002) and SDO continue today for the HXR and EUV ranges, respectively. Other missions that have contributed to our understanding of the solar x-ray spectrum, as listed in Figure 6.2, include the Solar and Heliospheric Observatorys (SOHO) Coronal Diagnostic Spectrometer (CDS), Hinodes EUV Imaging Spectrometer (EIS), GSAT-2s Solar X-ray Spectrometer (SOXS) Cadmium-Zinc-Telluride (CZT) and Si detectors, SMMs Bragg Crystal Spectrometer (BCS) and Flat Crystal Spectrometer (FCS), CGROs Burst and Transient Source Experiment (BATSE), Hinotoris solar Flare Monitor (FLM) and solar Soft X-ray Monitor (HXM), and P78-1s Solar X-rays (SOLEX) and X-ray Monitor (MONEX). With solar flare spectral variability expected to peak near 2 nm (Rodgers et al., 2006), in a range not currently observed by any spectrometer, MinXSS measurements of the solar SXR irradiance will provide a more complete understanding of flare variability in conjunction with measurements from RHESSI and EVE.

There are also nearly four decades of broadband (510 nm wide) SXR measurements not shown in Figure 6.2 because they do not provide spectrally resolved measurements. The very limited spectral information from these broadband measurements cannot quantify the specific spectral energy distribution, nor directly quantify the varying contributions of emission lines (bound-bound) among

the thermal radiative recombination (free-bound) and thermal and non-thermal bremsstrahlung (free-free) continua. These broadband measurements include, among others, the two geostationary operational environmental satellite (GOES) x-ray sensor (XRS) channels covering a combined band of 1.625 keV (0.05-0.8 nm) and the even broader band of 0.212 keV (0.1-7 nm) from several missions, including the Yohkoh soft x-ray telescope (1991-2001; Acton et al. 1999), Student Nitric Oxide Experiment (SNOE, 1998-2002; Bailey et al. 2000), Thermosphere-Ionosphere-Mesosphere Energetics and Dynamics (TIMED, 2002-present; Woods et al. 2005a), the Solar Radiation and Climate Experiment (SORCE, 2003-present; Woods et al. 2005b), and SDO (2010-present). Broadband measurements of solar SXRs have helped to resolve an outstanding difference between ionospheric models and measurements, such as the electron density from the Haystack Observatory incoherent scatter radar at Millstone Hill. In particular, the SNOE solar measurements were able to resolve the factor-of-4 difference between models and measurements because the SNOE data indicated much more SXR irradiance than had been previously thought (Solomon et al., 2001). Additional broadband SXR measurements have been made since then; however, differences still remain in understanding solar SXR spectral distribution and atmospheric photoelectron flux. Although smaller, these discrepancies are still as large as a factor of 2 at some wavelengths, as shown in Figure 6.3; the lack of spectral resolution in the SXR range is thought to be the culprit for most of these disagreements. For example, Peterson et al. (2009) show that discrepancy between photoelectron measurements and models were significantly improved with new EUV spectral measurements down to 6 nm, and we anticipate further improvement with new solar SXR spectral measurements and atmospheric modeling with data from the MinXSS because of its ability to measure all wavelengths in its spectral range simultaneously and with the relatively high spectral resolution of 0.15 keV full-width at half-maximum (FWHM).

6.2.1 Solar Flare Studies

Spectral models of the solar irradiance (e.g., CHIANTI; Dere et al. 1997; Landi et al. 2006) are needed to convert spectrally integrated broadband measurements into irradiance units. Detailed

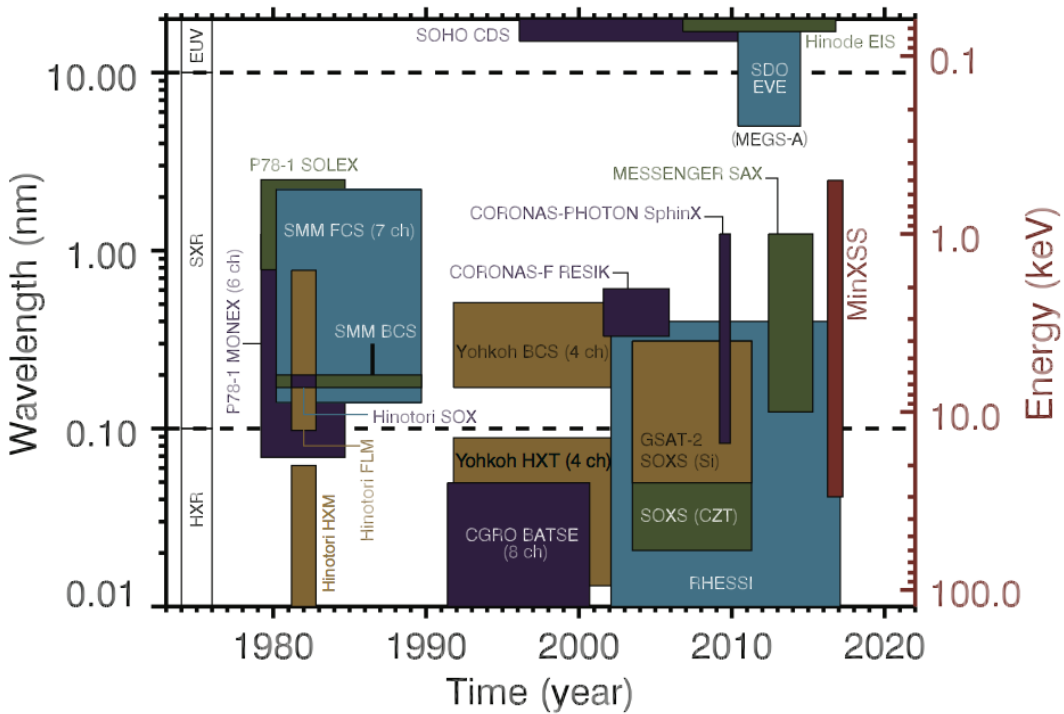


Figure 6.2: History of solar spectral measurements in and near soft x-ray energies (not exhaustive). Figure courtesy of Amir Caspi and Tom Woods.

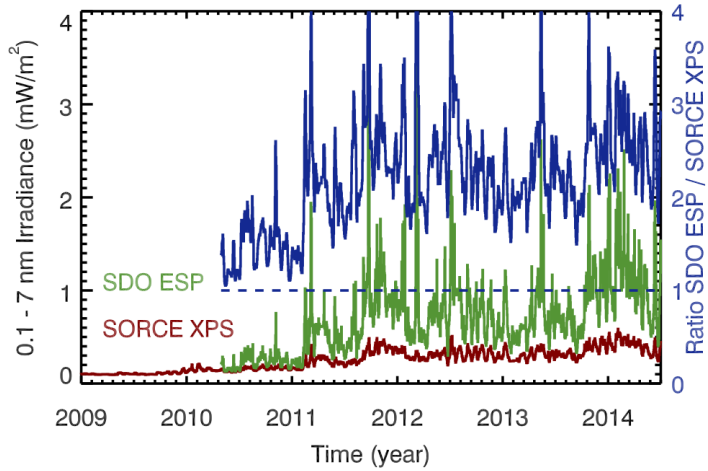


Figure 6.3: Solar 0.17 nm irradiance currently measured by broadband SXR photometers onboard NASA's SORCE and SDO satellites. Figure courtesy of Tom Woods.

modeling to estimate the SXR spectrum during a flare in April 2002 using a set of broadband measurements from the TIMED Solar EUV Experiment (SEE) was performed by Rodgers et al. (2006). The CHIANTI spectral model is part of their analysis and is also routinely used for processing these broadband measurements (e.g., Woods et al. 2008). Although the CHIANTI spectra are scaled to match the broadband SXR irradiance in data processing, there are significant differences for individual emissions lines between the CHIANTI model and observations, often more than a factor of 2 (Woods and Chamberlin, 2009; Caspi and Lin, 2010). Furthermore, there are concerns that CHIANTI could be missing many of the very hot coronal emissions lines, especially in the SXR range where there are so few spectral measurements between 0.5 and 6 nm. Additionally, there are factor of 2 differences when comparing the irradiance results from different broadband instruments, which are worst during times of higher solar activity (Figure 6.3). These discrepancies can be partially explained by wavelength-dependent instrument calibrations, but the greater contribution is likely the lack of knowledge of how this dynamic part of the solar spectrum changes as a function of wavelength and time.

The MinXSS spectrometer, an Amptek X123-SDD, flew on the EVE calibration rocket payload in June 2012, and that measurement had a difference of almost a factor of 8 below 2 nm as compared with the CHIANTI model prediction based on SORCE XPS broadband measurements (Caspi et al., 2015). This rocket result was a surprise considering that the SORCE-based CHIANTI model prediction agreed with SDO/EVE measurements down to 6 nm. Improvement of models of the solar SXR spectra, which is only possible with calibrated spectral measurements of the SXR emission, is critical to properly interpret these broadband measurements. Our goal with MinXSS observations is to reduce these SXR spectral differences from factors of 2 or more down to less than 30%. In addition, the MinXSS will measure solar SXR spectra with higher spectral resolution of 0.15 keV FWHM, as compared with the 0.6 keV FWHM resolution of the most recent analogous instrument, MESSENGER solar assembly for x rays (SAX; Schlemm et al. 2007). The MinXSS measurements will enable improvements to solar spectral models, such as CHIANTI and the Flare Irradiance Spectral Model (FISM; Chamberlin et al. 2007, 2008). By using the MinXSS to im-

prove the FISM predictions in the SXR range, atmospheric studies over the past 30 years will be possible, such as those for the well-studied Halloween 2003 storm period, as well as future space weather events after the MinXSS mission is completed. Getting this spectral distribution of solar flare energy in the SXR range is critical as a driver for atmospheric variations and will be discussed briefly in the next section.

The MinXSS data will also help improve understanding of the physics of solar flares themselves. The 0.5-9 keV (0.13-2.4 nm) range observed by the MinXSS is rich with high-temperature spectral lines from coronal plasma with temperatures from 5 to 50 million K, which are greatly enhanced during even small solar flares. MinXSS will also observe the underlying free-free and free-bound continua, extending out to 20-30 keV, which can provide an independent diagnostic of the emitting plasma temperatures. Understanding how solar flares heat plasma, especially up to many tens of million Kelvin, is a pressing question in solar physics (e.g., Caspi and Lin 2010; Fletcher et al. 2011; Caspi et al. 2014), and the MinXSS observations will provide the best spectral measurements in this energy range to date. Observing the variations of spectral lines in comparison with the continuum will also provide insight into coronal elemental abundances, particularly for Mg, Si, Fe, S, and Ar, to help measure abundances and to understand how they may vary with solar activity and during flares.

6.2.2 Topics Beyond Solar Eruptive Events

Quiescent-Sun Studies Examples of data analysis and spectral modeling for two quiescent (non-flaring) solar measurements made with the X123 aboard the EVE calibration rocket flights in 2012 and 2013 are provided in Caspi et al. (2015). One of the tantalizing results from these two 5 min observations is that the coronal abundance of certain elements is different for the quieter SXR spectrum on 2012 June 23 than the more active (but not flaring) sun on 2013 October 21. These abundance differences suggest that different heating mechanisms occur in the quiet network versus active regions and support the concept that numerous small impulsive events (“nanoflares,” e.g., Rodgers et al. 2006; Parker 1988) could be the source of the active region heating. Identifying

the mechanism responsible for heating the quiet sun corona to millions of degrees, while the photosphere below it is only 6000 K, remains one of the fundamental outstanding problems in solar physics (Klimchuk, 2006). We anticipate that one to three months of MinXSS measurements of the solar SXR spectrum will provide adequate data on active region evolution and several flares to more fully address these questions on nanoflare heating. The SXR variability is about a factor of 100-1000 over the solar cycle and can be as much as a factor of 10,000 for the largest X-class flares.

Improvements to Earth Atmospheric Models Energy from SXR radiation is deposited mostly in the ionospheric E region, from 80 to 150 km, but the altitude is strongly dependent on the incident solar SXR spectrum. This wavelength dependence is because of the steep slope and structure of the photoionization cross sections of atmospheric constituents in this wavelength range. The main reason that Earth's atmospheric cross section changes so dramatically in this range is because of the K edges of O at 0.53 keV (2.3 nm) and of N at 0.4 keV (3.1 nm). The distribution of energy in solar SXRs, even while holding total energy constant, results in peak energy deposition in Earth's atmosphere to change in altitude. The peak energy is near the mesopause but can vary by more than 5 km. This separation is considered significant because it is approximately equal to the scale height at 100 km, it is critical to E-region electrodynamics, and the mesopause (the coldest region of the atmosphere) is a critical transition between the middle and upper atmosphere.

6.3 Mission Architecture

All standard satellite subsystems are present on the MinXSS CubeSat, except for propulsion. Each will be overviewed in the following sections. Figure 6.4 shows the requirements flowdown from the science objectives to the mission level requirements, along with the expected performance of the system on orbit. Figure 6.5 shows the mechanical block diagram, and Appendix B shows the resource break-down of the spacecraft subsystems. Volume is only approximate because many components have nonstandard geometries. The 4800 g mass limit is derived from the interface control document for the NanoRacks CubeSat Deployer. The measurement requirement for range corresponds to the ISO standard definition for SXRs, and MinXSS is only required to make mea-

surements that fall somewhere within this range. The mission expectations listed are for FM-1 (ISS NanoRacks) only. The more conservative standard mass limit for a 3U CubeSat from the California Polytechnic State University CubeSat design specification is 4000 g and would result in a mass margin of 15% for the MinXSS.

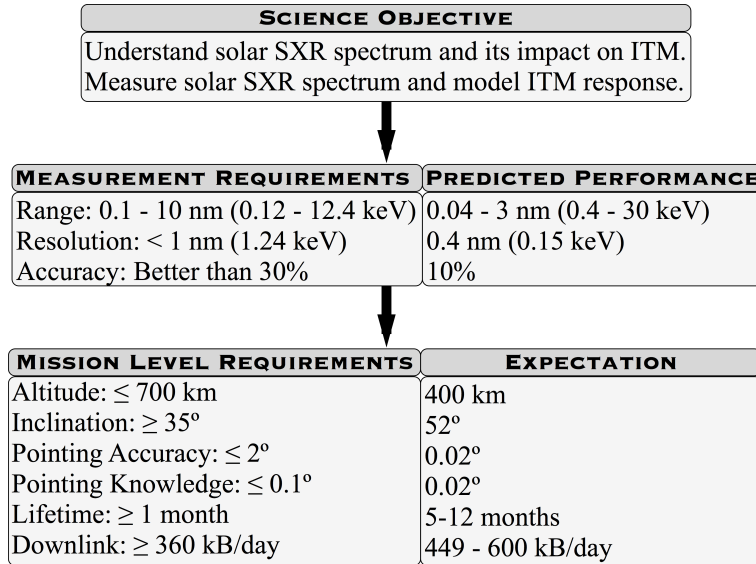


Figure 6.4: High-level requirements flowdown for MinXSS.

6.3.1 Primary Instrument: Amptek X123-SDD

The purpose of the primary MinXSS science instrument is to measure solar spectra within the International Organization for Standardization (ISO) standard SXR range of 0.1-10 nm listed in the requirements flowdown (Figure 6.4). To function within a CubeSat, the instrument must be low mass, low power, and have a small volume. A commercial off-the-shelf solution perfectly met these design requirements. The Amptek X123-SDD weighs 324 g after custom modifications were made for mounting to the CubeSat and thermal foam was added for cooling electrical components in vacuum. It consumes approximately 2.5 W of power nominally, and 5.0 W for approximately 1 min when first powered on. Much of the power draw (including the initial transient) results from the integrated thermoelectric cooler (TEC) reducing the temperature of the SDD to the user-

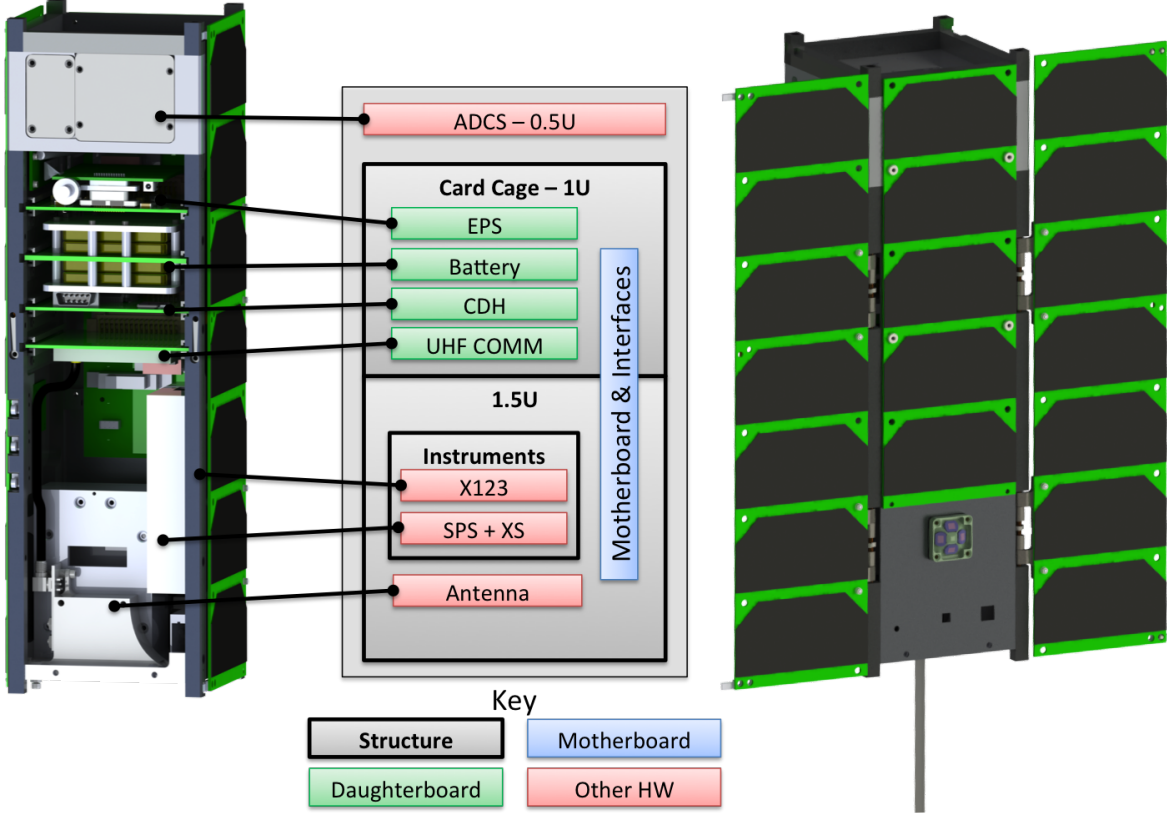


Figure 6.5: MinXSS CubeSat mechanical block diagram.

defined set point (-50 °C for the MinXSS). The dimensions of the X123 are also sufficiently small to easily fit within a CubeSat because of the manufacturers designed purpose as a handheld SXR measurement unit for geological fieldwork. The X123-SDD's 500 m active thickness and 16 m beryllium (Be) entrance window define a spectral range sensitivity of 0.430 keV (0.043 nm), which covers the primary range of interest for scientific studies of 0.52 nm. The instrument includes all the necessary processing electronics, including an integrated multichannel analyzer, to produce a spectrum that is output via an RS232 interface. It can also be commanded programmatically to change numerous parameters, such as integration time and energy thresholds. The custom modifications for spaceflight include staking the larger electronics components, adding a mounting plate for the electronics, adding a custom interface cable and 9-pin connector, adding a tungsten plate with pinhole aperture for the SDD, and providing stainless steel radiation shielding around

the aluminum detector vacuum housing.

In October 2014, the MinXSS science instruments, including the X123, were calibrated at the National Institute of Standards and Technology (NIST) Synchrotron Ultraviolet Radiation Facility (SURF; Arp et al. 2011). The synchrotron radiation provides a calibrated continuum emission source, with a radiometric accuracy of 10% in the SXR range. The SURF electron storage ring beam energy is adjustable from 60 to 416 MeV; the synchrotron spectral distribution is dependent on the beam energy, and the MinXSS calibrations use the higher beam energies to maximize the incident SXR flux. The absolute radiometric calibration of the X123, as a function of wavelength, is then obtained by comparing the measured output spectra with the known incident photon flux from the SURF beam; an example, and further description, can be found in Caspi et al. (2015). The narrow spatial extent of the SURF beam in the x-ray range allows for a mechanical determination of the instrument optical axis (“bore-sight”) relative to a reference frame, and the uniformity of response over the instrument’s field of view (FOV) is determined using a gimbal system to rotate the detector optical axis about the incident beam. The nonlinearity of the detector electronics is measured by adjusting the intensity of the incident synchrotron flux.

6.3.2 Secondary Instrument: Solar Position Sensor and X-Ray Sensor

The purpose of the secondary instrument is to provide support for scientific analysis of data from the primary instrument. Two sensors are needed to achieve this: one to provide independent high-precision attitude knowledge of the solar position and another to provide an in-flight SXR irradiance reference. Again, these instruments must be low mass, low power, and small volume to be accommodated within a CubeSat platform. MinXSS heavily leveraged instrument heritage from the larger GOES-R EUV x-ray irradiance sensor development at LASP, which already met all of these requirements. The custom-designed application specific integrated circuit (ASIC), in particular, provides the backbone of this exceptionally low-power, low-noise system. A custom mechanical design for the casing was necessary to integrate the subsystem with the MinXSS, which was manufactured for flight using aluminum sintering (3-D) printing.

Figure 6.6 shows an exploded mechanical view of this secondary instrument. The solar position sensor (SPS) is a quad-diode with effective neutral-density-7 filter and 2 mm^2 knife-edge aperture, with an FOV of 4° . The solar visible light falls on the four diodes such that the illumination on each diode depends on the incoming angle of the solar radiation. The resultant measurements are used to compute the sun's position to better than 1 arcmin (3σ) as described in Chamberlin et al. (2009). These data are sent to the attitude determination and control system (ADCS) for inclusion in the fine-attitude control solution and telemetered to the ground for use in science processing. The x-ray sensor (XS) is a single diode with two Be foil filters, whose total $16 \mu\text{m}$ thickness is matched to the X123 to define a response over the same 0.04-3 nm wavelength range. XS has a 5.0 mm diameter knife-edge aperture and an FOV of 4° . The diode operates in photocurrent mode, integrating the total SXR flux over its band-pass and integration period; this provides a measurement that can be compared with the integrated X123 spectrum, to within measurement and calibration uncertainties. These data are also telemetered to the ground for use in science data processing.

The SPS and XS were also calibrated at SURF. The SPS optical axis and the transfer equation relating off-axis position to quad-diode output were determined using the gimbal system to rotate the optical axis around the incident SURF beam. The XS optical axis and uniformity of response over its FOV were similarly determined. The absolute radiometric response of the XS was determined similarly to the X123, comparing the known incident synchrotron photon flux with the output from the photodiode. (No absolute calibration was necessary for the SPS.) The SPS and XS system, including ASIC, had been previously measured to be highly linear through testing during GOES-R development, and so the MinXSS calibrations omitted nonlinearity testing.

6.3.3 CDH and Flight Software

The core of the MinXSS CDH subsystem is a low-power Microchip dsPIC33 Microcontroller Unit (MC dsPIC33EP512MU810). The CDH communicates with and controls the X123 instrument, UHF communications, and ADCS via RS232, monitors voltages, currents, and temperatures

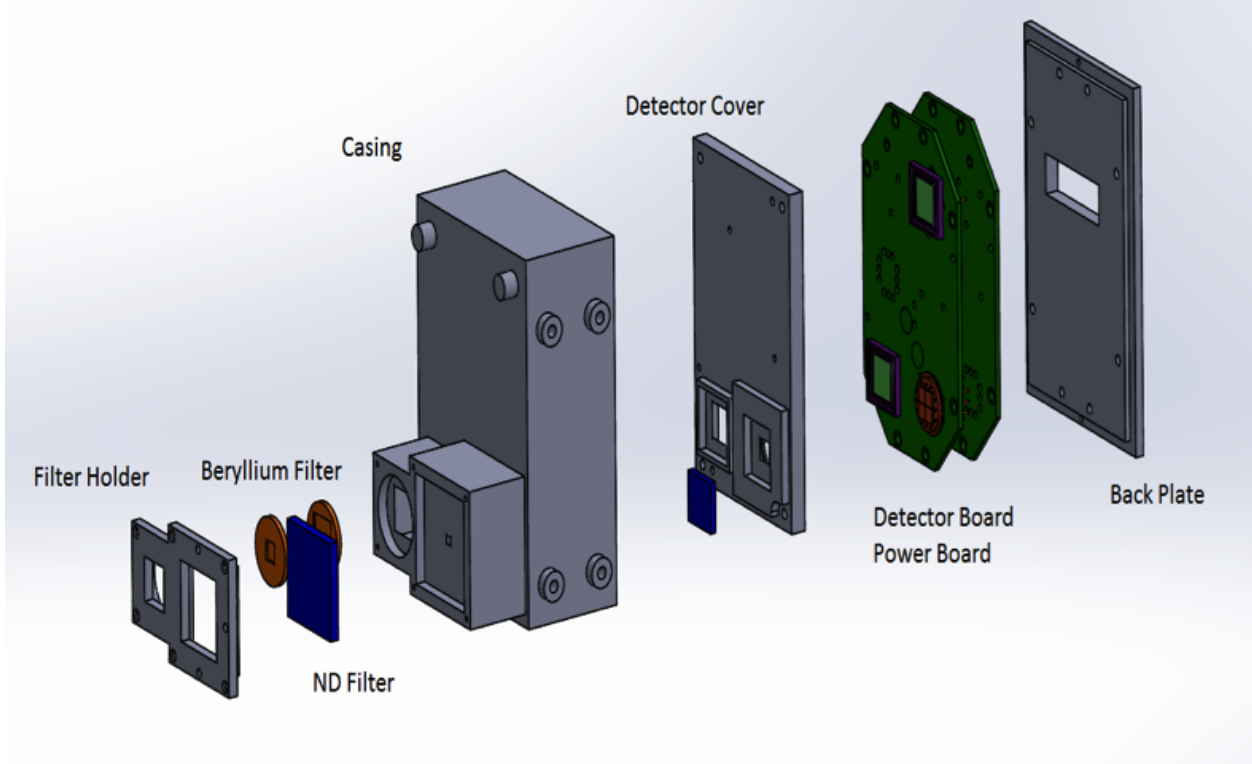


Figure 6.6: Solar position sensor and x-ray sensor (SPS and XS) exploded view. Figure courtesy of Siddhesh Naik.

via I2C for the motherboard, CDH, communications, EPS, and SPS and XS, and reads detector data from the SPS and XS ASIC via digital input/output. Additionally, the CDH handles all incoming commands, housekeeping monitoring, data manipulation for downlinking data packets, power switching of subsystems, and configuration of the operation modes. Most of the CDH operation is configurable via uplinked command, and several of these CDH processes are autonomous for maintaining a safe power configuration. Data are stored on a 4 GB secure digital (SD) memory card, and each type of data packet has its own dedicated circular buffer on the SD card. This SD card can store more than 1400 days (3.8 years) of science, housekeeping, and log message data packets, and 48 h of ADCS high-rate data packets. The dsPIC33 internal real-time clock (RTC) and an external RTC integrated circuit (IC) provide precise time knowledge. The external RTC IC also has an electrically erasable programmable read-only memory for storing startup configuration

parameters, which can be modified via uplinked commands. The dsPIC33 watchdog timer is used to initiate a reset of the system in case it becomes unresponsive, and a reset command can also be sent from the ground. The MinXSS FM-1 one year mission worst-case radiation dose estimate is 2.6 krad, with a minimum shielding of 2 mm of Al provided by the CubeSat structure. Two of the prototype CDH boards successfully passed radiation tests of 10 krad and 25 krad.

The embedded flight software is built on a Slot Real-Time Operating System (RTOS), written in C, as originally developed at LASP for the EVE rocket experiment. The key elements of the software design are robustness and simplicity, with the health and safety of the satellite as top priority. Because many of the tasks performed by the CDH are not time sensitive and can be handled at any time in the slot process, the real-time demands on the CDH and flight software are very low. The RTOS uses the dsPIC33 timer with 1 ms resolution for execution of tasks, but most monitoring by the CDH has a cadence of 1 s or slower.

6.3.4 Electrical Power System, Battery, and Solar Panels

The MinXSS EPS is largely based on heritage from the successful CSSWE direct energy transfer (DET) design. The EPS uses high-efficiency buck converters for power regulation to 3.3 and 5.0 V and a simple battery charging logic for use with Li-polymer batteries. Minor design modifications were incorporated to accommodate the higher power generation and consumption on the MinXSS as compared with CSSWE, as well as more voltage and current monitors. Two additional major differences were implemented: pseudo-peak power tracking (see Section 6.4.4) and additional switches to prevent the system being powered before deployment to comply with NanoRacks ISS human safety standards.

The battery pack consists of four SparkFun 2-Ah Li-polymer batteries, configured as two parallel sets of two batteries in series to provide a 6-8.4 V unregulated 4-Ah bus; two temperature sensors, and two heaters, which are sandwiched between the batteries. Heat transfer tape was used between each layer of the battery pack to achieve a homogenous temperature distribution during flight. The PCB in the middle of the pack does not have a copper plane in its center as all other

daughterboards do, the intent being to thermally isolate the batteries from the rest of the system. This was a part of the passive thermal design to create a battery-dedicated thermal zone, because the batteries have the narrowest operating temperature range of all components in the system. Finally, the pack was encapsulated with aluminum plates on standoffs, providing sufficient volume for the batteries to expand under vacuum and thermal cycling. Arathane 5753 with Cabosil glass beads was placed between the batteries and these encapsulation elements to act as a soft bumper to expanding batteries.

MinXSS uses 19 triple-junction GaAs, 30% efficient solar cells from Azur Space Solar Power, GmbH. One five-cell solar panel is fixed to the body of the CubeSat on the solar-oriented side, and two seven-cell solar panels will deploy by command to have the same solar orientation as the body-fixed panel. Because MinXSS is a sun-pointed spacecraft, these solar panels can nominally supply 22 W at end-of-life during the orbit insulation period. A 100 hour mission simulation test with the fully integrated spacecraft connected to a solar array simulator under various eclipse periods was performed to verify that there is adequate margin for operating all of the MinXSS subsystems and for charging the battery (see Section 6.4.5). Additionally, flight software incorporated the ability to autonomously power off the X123 (the largest power consuming subsystem) and the other non-critical subsystems during eclipse if there are any battery power issues for eclipse operations. The power-cycling flags can be enabled via command, but we do not anticipate the need for their use.

6.3.5 Communications

MinXSS leveraged heritage from the CSSWE CubeSat by using the same radio and ground station for UHF communications. The ground station is located on the roof of the LASP Space Technology Research Building in Boulder. It consists of a pair of M2 436CP42 cross Yagi antennas, each with a gain of 17 dB_{dc} and a circular beamwidth of 21°. A Yaesu G5500 azimuth-elevation rotator controlled by SatPC32 points the antenna system. SatPC32 also accounts for Doppler shifts via its control of the ground radio, a Kenwood TS-200. The antennas and motors are mounted on an 2.4 m tower and are connected to the electronics in the control room below by 60 m low-loss cabling,

which accrues 5.4 dBm of RF signal loss. The flight radio is an Astronautical Development, LLC Lithium-1 radio that operates in the UHF band at 437 MHz. Additionally, the antenna is nearly identical to that used on CSSWE, which is a deployable spring steel tape measure with a length of 47.6 cm. The gain pattern was measured using the MinXSS prototype in an anechoic chamber at First RF Corporation in Boulder, Colorado. The measurements were compared with a FEKO model and propagated through Satellite Tool Kit to estimate the expected daily average downlink data capacity: 600 kB day^{-1} using the FEKO model or 449 kB day^{-1} using the measurements. These estimates are not highly precise because of the limited fidelity of the model and the prototype structure, but provide an idea of what to expect. The requirement of at least 360 kB day^{-1} appears to be easily satisfied.

6.3.6 Attitude Determination and Control System

To provide a stable view of the sun for the science observations and to maintain appropriate antenna orientation during ground contacts, MinXSS has an active ADCS. With the wide field of view of the X123 (4°), the pointing requirements for MinXSS are only $2^\circ(3\sigma)$ accuracy and $0.1^\circ(3\sigma)$ knowledge.

The commercial CubeSat ADCS onboard the MinXSS is a flexible ADCS CubeSat technology (XACT) from Blue Canyon Technologies (BCT). BCT has developed a 0.5 U-sized ADCS unit (0.85 kg) using miniature reaction wheels, torque rods, a star tracker, a coarse sun sensor, inertial measurement units, and magnetometers. The BCT XACT is expected to provide pointing accuracy and knowledge of better than $0.003^\circ(1\sigma)$ in two axes, corresponding to the plane of sky of the star tracker, and $0.007^\circ(1\sigma)$ in the third axis, parallel to the star tracker optical axis. The XACT interface uses 5 and 12 V power inputs (1.0 W nominal, 2.8 W peak) and serial communication (RS232 for the MinXSS, but other options are available). SPS provides two-axis (pitch/yaw) pointing knowledge on the sun to better than 1 arcmin (3σ), which can be sent to the XACT for closed-loop fine-sun pointing; however, the XACT system can easily meet the MinXSS pointing requirements without this additional knowledge.

After integration with MinXSS, multiple tests were performed to verify functionality and performance of the ADCS. A custom air-bearing table was built to provide a relatively torque-free environment for the ADCS to control the spacecraft. For example, we verified that the spacecraft can track the sun with a heliostat at LASP, that magnetometers reversed sign when the spacecraft was rotated 180° in each axis, that torque rods produced a measurable magnetic field, and that the star tracker took interpretable images and found matches to stars in its library when observing the night sky.

6.4 Advancing CubeSat Technologies and Lessons Learned

6.4.1 CubeSat Card Cage



Figure 6.7: Prototype CubeSat card cage design. Figure courtesy of Tom Woods.

Experience with the PC104 PCB interface on the CSSWE CubeSat led the MinXSS team away from the card stack design because of the difficulty in debugging boards once integrated. Instead, the CubeSat card cage design uses a motherboard/daughterboard architecture that allows any individual card to be easily removed, and an extender board optionally inserted to have access

to the daughterboard for probing while still electrically connected (Figure 6.7). Additionally, the standard electrical interface allows boards to be swapped to any position. MinXSS uses a DIN 48-pin connector for the daughterboard/motherboard interface. This relatively large connector was chosen for ease of soldering for new engineering students and because it easily satisfied the requirements on the number of necessary pins and mechanical dimensions. In the future, a higher density connector with potentially more pins could be chosen to provide a lower mass and lower volume solution while still providing the flexibility of the card cage architecture.

6.4.2 3-D Printed Parts

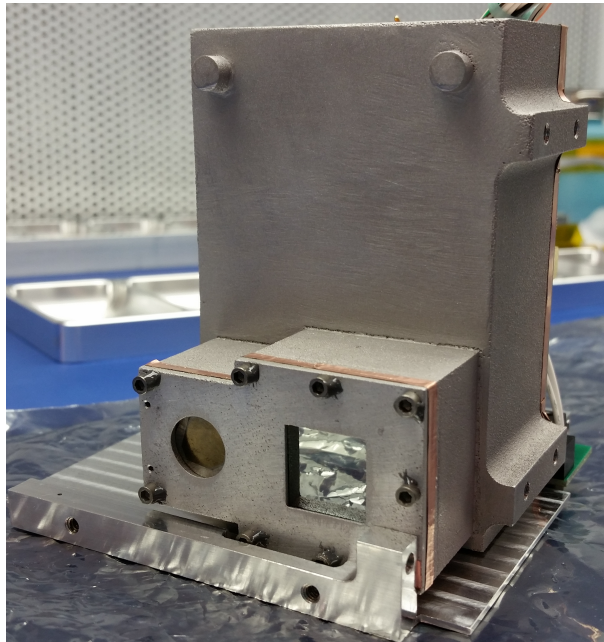


Figure 6.8: Aluminum 3-D printed SPS and XS housing after sanding and integration.

The MinXSS project used 3-D printed parts for both prototyping and flight components. For prototyping, the SPS and XS housing was 3-D printed in plastic twice as the design iterated, and the solar array hinges were printed in plastic once. This was done using CU's Objet 30 printer with VeroWhitePlus plastic. For flight, these same components were 3-D printed in metal using direct metal laser sintering at GPI Prototype. The SPS and XS housing is aluminum with a shot-blasted

finish (Figure 6.8). This finish was very rough and required significant sanding to get an acceptable surface finish and clean edges. The solar array hinges are stainless steel with a shot-blasted finish (Figure 6.9). A minimal amount of sanding was required for these parts because the requirements were looser and the finish was slightly better than SPS and XS. The better finish was likely because of the hinges being a simpler part that required no filler material during the 3-D print (sintering) process.

As plastic 3-D printers become more pervasive, affordable, and precise, the draw toward using the resultant parts for flight is becoming stronger. A major risk that must be addressed is the unknown properties of these materials, particularly in their response to vacuum and UV exposure. We would like to see an open database where specifications based on test results for common 3-D print materials, such as ABS and PLA, could be accessed.



Figure 6.9: Stainless steel 3-D printed solar array hinges as delivered from vendor.

6.4.3 Simplification of Solar Panel Fabrication Process

CSSWE used epoxy (Arathane 5753) on the back of solar cells to adhere them to the solar panel PCBs. This technique is typical but requires significant assembly and curing time. MinXSS used double-sided Kapton tape with acrylic adhesive to adhere solar cells to the PCBs. We used a specialized rubber vacuum sealer to apply pressure to the cells uniformly and meet the manu-

facturers recommended application pressure. This reduced the time to produce a solar panel from three days to one day. To get electrical conductivity from the back of the solar cell to the PCB, we applied silver epoxy in large vias behind each cell. We also tested a new-to-market tape: 3M Z-axis tape. This tape is electrically conductive between the adhesive and backside and could save the extra step of applying the silver epoxy or soldering/welding on tabs. For flight, Kapton tape was used because 1) the Z-axis tape adhesive was not rated for as wide a temperature range as the Kapton acrylic adhesive, 2) there was concern that the Z-axis tape could not sustain the high current of the solar cells for as long as solder or silver epoxy could, and 3) the Z-axis tape thermal conductivity properties were not specified in the datasheet. In the future, we would like to see solar cell manufacturers adopt a standard form factor compatible with CubeSats. MinXSS uses 40 x 80 mm cells from Azur Space (Figure 6.10), which are a great fit within the rail boundaries of CubeSats (maximum of 83 mm wide and 340.5 mm long for 3U CubeSat). The 80 mm width for cells provides a 1.5 mm margin on each side from the rails. If the spacing between cells could be reduced to 4.5 mm or less, then there could be eight Azur Space solar cells instead of seven on a 3U panel. Alternatively, if the height of the cells were changed to be 50 mm instead of 40 mm, then they would be more modular for fitting one solar cell per 0.5U of the panel length. With six 50 x 80 mm cells instead of seven 40 x 80 mm cells, there could be 7% more power per 3U panel.

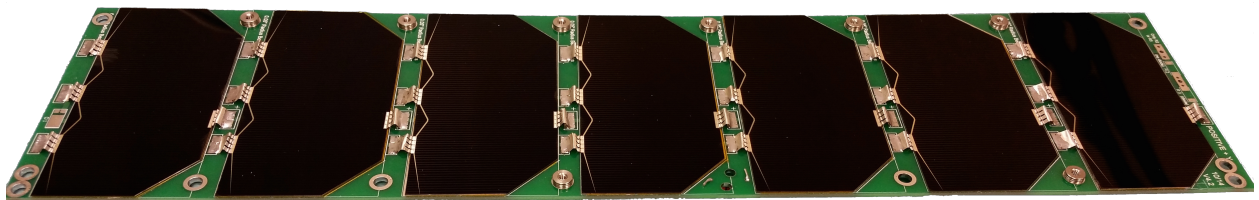


Figure 6.10: Populated seven-cell deployable solar array for MinXSS FM-1.

6.4.4 Pseudo-Peak Power Tracking

A modified DET EPS design was implemented on MinXSS that was inherited from the CSSWE CubeSat to include an additional specially selected resistor to create a pseudo-peak power

tracking (PPPT) system. The extra resistor was chosen to prevent a rapid voltage drop from the solar cells when the battery attempts to draw a large current, namely, when the battery state of charge is relatively low right as the spacecraft exits the orbit eclipse.

In the CSSWE and MinXSS EPS design, the output of the solar panels power 8.6 V regulators that then provide regulated 8.5 V power directly to the battery and system. In this DET design, the batteries will charge up to 8.5 V, and there are no supporting electronics required to control the battery charging process. In reality, this simple approach only provides about 50% of the power intended from the solar panels when the battery capacity is low. In particular, when the battery needs more power input (high current) for charging, the high current draw from the solar cells results in much lower voltage, following the standard solar cell current-voltage I-V curve. When the solar panel output voltage goes below the minimum input voltage level of the 8.6 V regulator, the regulator turns off. Consequently, the current drops and the solar panel output voltage increases, and the 8.6 V regulator turns back on. This results in a high-frequency on-off regulator oscillation that had the EPS 8.6 V regulators on for only about 50% of the time during the early part of the orbit dayside during mission simulations. The MinXSS solar panels were designed for 80% of peak efficiency at EOL, but the 50% decrease in power was an unacceptable power loss for the nominal power budget.

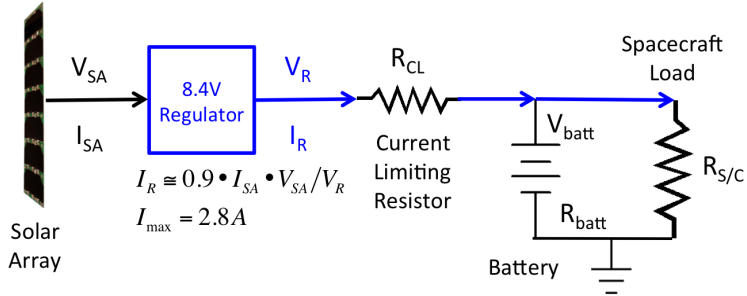


Figure 6.11: Simplified circuit diagram of PPPT for MinXSS EPS. Figure courtesy of Tom Woods.

The solution for MinXSS, without having to redesign or rebuild the EPS board, was to replace the sense resistor on the output of the solar panel regulator with a larger resistance so

that the effective current draw out of the solar panel would be limited and thus would not cause the regulator to turn off. We refer to this current-limiting resistor for the solar panels as PPPT. Figure 6.11 shows a simplified version of the PPPT circuit for the MinXSS EPS. The value for this current-limiting resistor was estimated for the MinXSS power configuration using Equation 6.1.

$$I_{Reg} = \frac{V_{Reg} - I_{max}R_{CL}}{R_{S/C}} + \frac{V_{Reg} - I_{max}R_{CL} - V_{Batt}}{R_{CL} + R_{Batt}} \quad (6.1)$$

where I_{Reg} is the current output from the regulating buck converter, V_{Reg} is the corresponding voltage, I_{max} is the maximum current from the solar panel, R_{CL} is the resistance of the current-limiting resistor for pseudo-peak power tracking, $R_{S/C}$ is the spacecraft load, V_{Batt} is the voltage of the battery pack, and R_{Batt} is the resistance of the battery pack.

The first term on the right-hand side of Equation 6.1 is the current for the spacecraft load, and the second term is the current for charging the battery. The spacecraft load is assumed to be constant, but the battery charging current starts off high when the battery voltage is low and then ramps down to zero when the battery voltage is the same as the regulator voltage downstream of the current-limiting resistor. The ideal value for the current-limiting resistor R_{CL} is such that it limits the current out of the regulator I_{Reg} to be less than the maximum current I_{max} possible from the regulator (at the peak power part of the solar panel I-V curve) and when the battery voltage V_{batt} is at the lowest allowed level. For MinXSS design and configuration, the regulator voltage V_{Reg} is 8.5 V, the worst-case system load (largest power) has 7.0 Ω for R_{SC} , a battery impedance of 0.125 Ω, and a value of 2.8 A for I_{max} . The goal for MinXSS was to keep the battery voltage above 7.1 V at all times, and so an R_{CL} of 0.25 Ω is the desired value for the MinXSS configuration to satisfy Equation 6.1. That is, with this value of R_{CL} , I_{Reg} equals I_{max} when V_{batt} equals 7.1 V. After the current-limiting resistor was installed into the EPS, additional mission simulations were run. We verified that the prediction of the regulator current I_{Reg} and the measured battery voltage agreed with the measured regulator current.

One disadvantage to the PPPT implementation is that there is additional heating of the

EPS board because of the larger resistance; however, this extra heating peaks right after exiting eclipse, the precise time when temperatures are cooler and heating is desired anyway. For example, the power loss (heating) in the PPPT current-limiting resistor is estimated to be 2.6 W when the battery voltage is at its lowest value of 7.1 V, decreasing to 0.93 W when the battery voltage is at 7.5 V, and reduces to less than 0.1 W once the battery voltage is above 8.0 V. The primary caveat in the PPPT design is that resistor tuning must be done a priori, and is fixed, whereas maximum PPT (MPPT) systems can tune resistance in real time to maintain the maximum power point on the solar cell I-V curve. The trade studies performed for CSSWE and MinXSS resulted in the selection of a custom DET EPS because of the simplicity of design. Both teams were unaware of the consequential loss of power generation at the time of the original designs. The advantage of the PPPT circuit is that it is only minimally more complex than DET, adding little risk for a large benefit.

In the future, we would like to see a standard MPPT IC for interfacing to common CubeSat battery packs (e.g., 8.4 V Li-polymer battery packs). We found it difficult to identify a commercial MPPT IC or proven MPPT circuit that could be integrated with our system. We purchased the most promising MPPT IC, a Linear Technology LT3652, and spent significant time attempting to integrate it with the MinXSS EPS, but its intended use prevented proper functioning for our solar panel and battery configuration.

6.4.5 Importance of Flight Like Testing

Various tests were performed on MinXSS that were geared toward simulating the orbital environment and flight-like operations. These included low-external-torque tests of the ADCS, thermal vacuum with a long-duration mission simulation, early orbit end-to-end communication testing performed several miles away from the ground station, and detailed battery characterization of the actual batteries to be flown.

Using a custom-built air-bearing table, we tested the functionality and performance of the ADCS. This test simulated an orbital environment with reduced external torques present. Through

this testing, we discovered that an operational amplifier (op-amp) was preventing the XACT coarse sun sensor from being properly read by its internal flight software, and this op-amp was replaced to resolve this issue. It is unlikely this would have been discovered otherwise and may have resulted in the spacecraft not being able to quickly find or accurately track the sun while on orbit. Significant effort in mission operations may have been able to salvage the mission in that situation, but only minor effort was required to replace the offending op-amp. Air-bearing testing requires very careful balancing of the system and as much reduction of external torques as possible (e.g., even airflow from building ventilation could limit the tracking duration while operating on the air-bearing table). It also requires the computation of moments of inertia specific to the air-bearing CubeSat system to be provided to the ADCS for appropriate control to be implemented. Without such an update to the ADCS software, the ADCS response is too sluggish (slow) to confirm that the ADCS is tracking as expected.

Thermal vacuum tests are irreplaceable for determining if the CubeSat can function in vacuum and for measuring performance near the operational limits of components. Through such testing of MinXSS, we discovered a short in a battery heater that reset the entire system every few seconds, which only manifested under vacuum. This was caused by the battery expansion, which created an unintended electrical connection between the two nodes of the heater. Typically, CubeSats are only required to bake out, not perform a functional thermal vacuum test, but we highly recommend this test as a process to increase the success rate of CubeSats.

A 100 hour mission simulation test was performed on MinXSS during four of the eight hot/cold cycles of the thermal vacuum testing. A solar array simulator, with an I-V curve programmed to model the Azur Space solar cells used on the MinXSS, was jumpered into the MinXSS EPS board. The jumper bypassed the two deployable solar panels. The output of the solar array simulator was programmatically cycled in intervals corresponding to ISS orbit insolation/eclipse periods at three different β angles. The total orbit period was 93 min and the three eclipse periods were 28 min (average β), 38 min ($\beta = 0^\circ$), and 0 min ($\beta > 76^\circ$). Power performance data were collected for the entire system throughout each of these scenarios and verified that the PPPT maintained a power

positive state through many orbits. Additionally, this test was used to verify the functionality of a flight software commandable flag to disable power to the X123 during eclipse periods. This option was introduced into the flight software early in the project in anticipation of a marginal power balance. The X123 was chosen for power cycling because it is the largest consumer of power and because the primary science target (the sun) is not visible in eclipse. However, this is not the default state in the mission design because it introduces excessive power cycling on the primary science instrument; nominal operations leave the X123 powered on during the entire orbit. As the spacecraft performance degrades on orbit (e.g., solar cell efficiency loss), it may become necessary to enable the X123-eclipse-power-cycling flag. Finally, the 100 hour mission simulation test included periodic stored-data downlinking with durations equivalent to the ground station contacts expected on orbit. The 100 hour mission simulation test was the most flight-like testing possible with the facilities available and greatly increased confidence in and understanding of the system as it will behave on orbit. It also ensured that the flight electronics are likely past the “infant mortality” phase.

End-to-end testing was also performed on the MinXSS to verify functionality of the full communication pipeline. The spacecraft was taken several miles away to a position in the line-of-sight of the ground station, and early orbit commissioning tests were performed. This boosted confidence in several areas: that we would meet the NanoRacks requirement of not deploying the MinXSS antenna or solar arrays in the first 30 min after deployment from the ISS, that those deployments would be successful, that communications could be established after antenna deployment, and that our ground software commissioning scripts could autonomously perform telemetry verification and commanding.

Significant battery testing was performed to comply with requirements flowed down from NASA Johnson Space Center through NanoRacks to all CubeSats going to the ISS. These requirements are in place to protect astronauts on the ISS and far exceed the standard CubeSat requirements in the California Polytechnic State University CubeSat Design Specification. Nevertheless, we recommend that all CubeSats perform several of these tests, if only to better understand

the actual batteries to be flown (i.e., not just batteries from the same lot or of the same type). We found the following to be the most useful tests: visual inspection for dents or leaks, measuring the open circuit voltage of the fully configured battery pack, recording voltage, current, and temperature through three charge/discharge cycles; measuring the voltages at which overcharge and overdischarge protection activated and deactivated; and measuring mass before and after undergoing vacuum. Given availability of the equipment to perform these tests and measurements, it took approximately two weeks to complete this testing for each battery pack. Much of that time was dedicated to setup, waiting for charge cycles to complete, and interpretation of the results. Additional tests were required for astronaut safety on the ISS, but we would consider them to be extraneous for non-ISS CubeSat missions. These include measuring of the physical dimensions of each battery, measuring the closed circuit voltage of the fully configured battery pack, measuring the time to trigger short-circuit protection and maintaining the short for 3 hours to verify the protection remains enabled; and doing a dedicated vibration test at five frequencies and strengths up to $9.65\ g_{rms}$ on all three axes, with voltage measurements between each axis. These additional tests took several weeks of additional time and planning, particularly in the design, manufacturing, and modification of components to support vibration testing.

6.4.6 Importance of a Second CubeSat Unit

The fabrication of two identical sets of hardware in parallel is much less expensive than the same development in series, particularly if the start of the development for the second set is delayed by months or years. Small projects tend to have less stringent requirements on documentation, and so details can be forgotten and lost in the time between two sets of flight hardware developed in series. Having two sets of hardware enables the development and testing of flight software, while other activities proceed in parallel. It is important to note that parallel development also enables the replacement of a subsystem if a problem is found, which is critical when schedules are tight. This was the case for the MinXSS when the battery heater short was discovered in FM-1 at the initial pump down for its thermal vacuum test. We were delayed half a day to swap the battery

pack out with FM-2, which did not have the same issue, as compared with the weeks of delay that would have been introduced if an entirely new battery pack had to be assembled and tested. Finally, having a second flight unit allows for debugging of hardware and software after delivery and launch of the first flight unit.

6.4.7 Low-Cost Mitigation of Radiation Issues for Electronics

The CubeSats developed at CU and LASP have generally used industrial-grade (automobile) electronic parts because those parts have wider operating temperature ranges. Typically, the automobile-grade ICs cost \$ 10 as compared with \$ 2 for standard commercial ICs, but this additional cost is outweighed by the significant benefits of the higher-grade components. For example, the number of uncorrupted SD card write cycles can be improved by a factor of 10100, and the operational temperature range can be expanded by purchasing a \$ 70 4 GB hardened SD card instead of a \$ 4 standard SD card. The total cost impact on the MinXSS for these industrial-grade electronics parts is only a few thousand dollars, a small fraction of the total budget, but it significantly improves the potential for a longer mission life. Although our intention was to have electronics that could operate over a wider temperature range, automobile-grade parts may also help with radiation tolerance of the electronics. Two MinXSS prototype CDH boards were radiation tested, one to 10 krad and another to 25 krad; both boards survived. It is not clear if industrial-grade parts made a difference or not for passing the harder radiation test; nonetheless, it is only a small cost increment to use the higher-grade parts.

6.5 Summary

CubeSat technologies and capabilities are now sufficiently mature to enable peer-review journal-quality science missions. This was clearly proven with the CSSWE CubeSat, which has 17 such articles to date (Li et al., 2012; Gerhardt et al., 2013; Li et al., 2013b,a, 2015; Baker et al., 2014; Jaynes et al., 2014; Schiller et al., 2014a,b; Blum et al., 2013; Blum and Schiller, 2012; Kohnert et al., 2011; Palo et al., 2010; Schiller and Mahendrakumar, 2010; Gerhardt, 2010; Gerhardt

and Palo, 2016a,b). Leveraging that success and the recent development of a commercially available, precision three-axis ADCS, MinXSS will push the boundary of what science is possible with a CubeSat further still. The primary science objective of MinXSS is to fill a critical spectral gap in solar measurements currently made by large satellite missions at one hundredth their typical cost. All standard satellite subsystems are present in the MinXSS, except propulsion, packaged in a volume that can fit in a breadbox. Many of these subsystems were custom developed by CU and LASP (e.g., CDH, EPS, SPS, and XS, structure), primarily by graduate students with professional mentorship; and other subsystems were purchased from commercial vendors (e.g., flight radio, ADCS, primary science instrument).

Bibliography

- Acton, L. W., Weston, D. C., and Bruner, M. E. (1999). Deriving solar X ray irradiance from Yohkoh observations. *Journal of Geophysical Research*, 104(A7):14827.
- Andretta, V., Del Zanna, G., and Jordan, S. D. (2003). The EUV helium spectrum in the quiet Sun: A by-product of coronal emission? *Astronomy and Astrophysics*, 400(2):737–752.
- Arp, U., Clark, C., Deng, L., Faradzhev, N., Farrell, A., Furst, M., Grantham, S., Hagley, E., Hill, S., Lucatorto, T., Shaw, P.-S., Tarrio, C., and Vest, R. (2011). SURF III: A flexible synchrotron radiation source for radiometry and research. *Nuclear Instruments and Methods in Physics Research Section A: Accelerators, Spectrometers, Detectors and Associated Equipment*, 649(1):12–14.
- Aschwanden, M. J. (2009). 4-D modeling of CME expansion and EUV dimming observed with STEREO/EUVI. *Annales Geophysicae*, 27(8):3275–3286.
- Aschwanden, M. J., Nitta, N. V., Wuelser, J.-P., Lemen, J. R., Sandman, A., Vourlidas, A., and Colaninno, R. C. (2009a). First Measurements of the Mass of Coronal Mass Ejections From the EUV Dimming Observed With Stereo EUVI A + B Spacecraft. *The Astrophysical Journal*, 706(1):376–392.
- Aschwanden, M. J., Wuelser, J. P., Nitta, N. V., and Lemen, J. R. (2009b). Solar Flare and CME Observations with STEREO/EUVI. *Solar Physics*, 256(1-2):3–40.
- Attrill, G. D. R., Harra, L. K., van Driel-Gesztelyi, L., and Wills-Davey, M. J. (2010). Revealing the Fine Structure of Coronal Dimmings and Associated Flows with Hinode/EIS. *Solar Physics*, 264(1):119–147.
- Bailey, S. M., Woods, T. N., Barth, C. A., Solomon, S. C., Canfield, L. R., and Korde, R. (2000). Measurements of the solar soft X-ray irradiance by the Student Nitric Oxide Explorer : First analysis and underflight calibrations. *Journal of Geophysical Research*, 105:27179–193.
- Baker, D. N., Jaynes, A. N., Hoxie, V. C., Thorne, R. M., Foster, J. C., Li, X., Fennell, J. F., Wygant, J. R., Kanekal, S. G., Erickson, P. J., Kurth, W., Li, W., Ma, Q., Schiller, Q., Blum, L., Malaspina, D. M., Gerrard, A., and Lanzerotti, L. J. (2014). An impenetrable barrier to ultrarelativistic electrons in the Van Allen radiation belts. *Nature*, 515(7528):531–4.
- Bein, B. M., Temmer, M., Vourlidas, A., Veronig, A. M., and Utz, D. (2013). THE HEIGHT EVOLUTION OF THE TRUE CORONAL MASS EJECTION MASS DERIVED FROM STEREO COR1 AND COR2 OBSERVATIONS. 31.

- Bevington, P. (2003). *Data reduction and error analysis for the physical sciences*. McGraw-Hill, Boston.
- Bewsher, D., Harrison, R. A., and Brown, D. S. (2008). The relationship between EUV dimming and coronal mass ejections I. Statistical study and probability model. *Astronomy & Astrophysics*, 478:897–906.
- Blum, L. and Schiller, Q. (2012). Characterization and Testing of an Energetic Particle Telescope for a CubeSat Platform.
- Blum, L. W., Schiller, Q., Li, X., Millan, R., Halford, A., and Woodger, L. (2013). New conjunctive CubeSat and balloon measurements to quantify rapid energetic electron precipitation. *Geophysical Research Letters*, 40(22):5833–5837.
- Caspi, A. and Lin, R. P. (2010). RHESSI Line and Continuum Observations of Super-hot Flare Plasma. *The Astrophysical Journal*, 725:L161–166.
- Caspi, A., McTiernan, J. M., and Warren, H. P. (2014). CONSTRAINING SOLAR FLARE DIFFERENTIAL EMISSION MEASURES WITH EVE AND RHESSI. *The Astrophysical Journal*, 788(2):L31.
- Caspi, A., Woods, T. N., and Warren, H. P. (2015). New Observations of the Solar 0.55 Kev Soft X-Ray Spectrum. *The Astrophysical Journal*, 802(1):L2.
- Chamberlin, P. C., Woods, T. N., and Eparvier, F. G. (2007). Flare Irradiance Spectral Model (FISM): Daily component algorithms and results. *Space Weather*, 5(7):n/a–n/a.
- Chamberlin, P. C., Woods, T. N., and Eparvier, F. G. (2008). Flare Irradiance Spectral Model (FISM): Flare component algorithms and results. *Space Weather*, 6(5):n/a–n/a.
- Chamberlin, P. C., Woods, T. N., Eparvier, F. G., and Jones, A. R. (2009). *Next generation x-ray sensor (XRS) for the NOAA GOES-R satellite series*. In Fineschi, S. and Fennelly, J. A., editors, *SPIE Optical Engineering + Applications*, pages 743802–743802–10. International Society for Optics and Photonics.
- Chen, P. F., Fang, C., and Shibata, K. (2005). A Full View of EIT Waves. *The Astrophysical Journal*, 622(2):1202–1210.
- Chen, P. F., Wu, S. T., Shibata, K., and Fang, C. (2002). Evidence of EIT and Moreton Waves in Numerical Simulations. *The Astrophysical Journal*, 572(1):L99–L102.
- Colaninno, R. C. and Vourlidas, A. (2009). First Determination of the True Mass of Coronal Mass Ejections: A Novel Approach To Using the Two Stereo Viewpoints. *The Astrophysical Journal*, 698:852–858.
- Colaninno, R. C., Vourlidas, A., and Wu, C. C. (2013). Quantitative comparison of methods for predicting the arrival of coronal mass ejections at Earth based on multiview imaging. *Journal of Geophysical Research: Space Physics*, 118(11):6866–6879.
- Dere, K. P., Landi, E., Mason, H. E., Monsignori Fossi, B. C., and Young, P. R. (1997). CHIANTI - an atomic database for emission lines. *Astronomy and Astrophysics Supplement Series*, 125:149–173.

- Doschek, G. A. (1990). Soft X-ray spectroscopy of solar flares - an overview. *The Astrophysical Journal Supplement Series*, 73:117.
- Fletcher, L., Dennis, B. R., Hudson, H. S., Krucker, S., Phillips, K., Veronig, A. M., Battaglia, M., Bone, L., Caspi, A., Chen, Q., Gallagher, P. T., Grigis, P. T., Ji, H., Liu, W., Milligan, R. O., and Temmer, M. (2011). An Observational Overview of Solar Flares. *Space Science Reviews*, 159(1-4):19–106.
- Gerhardt, D. (2010). Passive Magnetic Attitude Control for CubeSat Spacecraft.
- Gerhardt, D. and Palo, S. (2016a). Volume Magnetization for System-Level Testing of Magnetic Materials within Small Satellites.
- Gerhardt, D. and Palo, S. E. (2016b). Passive Magnetic Attitude Control Settling Prediction with On-Orbit Verification using the Colorado Student Space Weather Experiment CubeSat.
- Gerhardt, D., Palo, S. E., Schiller, Q., Blum, L., Li, X., and Kohnert, R. (2013). The Colorado Student Space Weather Experiment (CSSWE) On-Orbit Performance. *Journal of Small Satellites*, 3(1):265–281.
- Gilbert, H. R., Inglis, a. R., Mays, M. L., Ofman, L., Thompson, B. J., and Young, C. a. (2013). Energy Release From Impacting Prominence Material Following the 2011 June 7 Eruption. *The Astrophysical Journal*, 776(1):L12.
- Giordano, S., Antonucci, E., and Dodero, M. (2000). OXYGEN VELOCITIES IN A POLAR CORONAL. *Advances in Space Research*, 25(9):1927–1930.
- Gopalswamy, N., Yashiro, S., Michalek, G., Stenborg, G., Vourlidas, A., L, F. S., and Howard, R. A. (2009). The SOHO / LASCO CME Catalog. *Earth Moon Planet*, 104:295–313.
- Greenstein, J. L. (1958). High-Resolution Spectra of Comet MRKOS. *The Astrophysical Journal*, 128:106.
- Harra, L. K., Mandrini, C. H., Dasso, S., Gulisano, A. M., Steed, K., and Imada, S. (2010). Determining the Solar Source of a Magnetic Cloud Using a Velocity Difference Technique. *Solar Physics*, 268(1):213–230.
- Harra, L. K. and Sterling, A. C. (2001). Material Outflows from Coronal Intensity "Dimming Regions" During Coronal Mass Ejection Onset. *The Astrophysical Journal Letters*, 561:215–218.
- Harrison, R. A., Bryans, P., Simnett, G. M., and Lyons, M. (2003). Coronal dimming and the coronal mass ejection onset. *Astronomy & Astrophysics*, 400:1071–1083.
- Harrison, R. A. and Lyons, M. (2000). A spectroscopic study of coronal dimming associated with a coronal mass ejection. *Astronomy & Astrophysics*, 310:1097–1108.
- Hudson, H. S., Lemen, J. R., St. Cyr, O. C., Sterling, A. C., and Webb, D. F. (1998). X-ray coronal changes during halo CMEs. *Geophysical Research Letters*, 25(14):2481–2484.
- Hudson, H. S., Woods, T. N., Chamberlin, P. C., Fletcher, L., Zanna, G. D., Didkovsky, L., Labrosse, N., and Graham, D. (2011). The EVE Doppler Sensitivity and Flare Observations. *Solar Physics*, 273:69–80.

- Hyder, C. L. and Lites, B. W. (1970). H-alpha Doppler Brightening and Lyman-alpha Doppler Dimming in Moving H-alpha Prominences. *Solar Physics*, 14(1):147–156.
- Imada, S., Hara, H., Watanabe, T., Kamio, S., Asai, A., Matsuzaki, K., Harra, L. K., and Mariska, J. T. (2007). Discovery of a Temperature-Dependent Upflow in the Plage Region during a Gradual Phase of the X-Class Flare. *Publications of the Astronomical Society of Japan*, 59(sp3):S793–S799.
- Jaynes, A. N., Li, X., Schiller, Q. G., Blum, L. W., Tu, W., Turner, D. L., Ni, B., Bortnik, J., Baker, D. N., Kanekal, S. G., Blake, J. B., and Wygant, J. (2014). Evolution of relativistic outer belt electrons during an extended quiescent period. *Journal of Geophysical Research: Space Physics*, 119(12):9558–9566.
- Jin, M., Ding, M. D., Chen, P. F., Fang, C., and Imada, S. (2009). CORONAL MASS EJECTION INDUCED OUTFLOWS OBSERVED WITH HINODE /EIS. *The Astrophysical Journal*, 702(1):27–38.
- Kahler, S. (1992). Solar Flares and Coronal Mass Ejections. *Annual Review of Astronomy and Astrophysics*, 30:113–141.
- Kahler, S. W. (1982). The role of the big flare syndrome in correlations of solar energetic proton fluxes and associated microwave burst parameters. *Journal of Geophysical Research*, 87(A5):3439.
- Klimchuk, J. A. (2006). On Solving the Coronal Heating Problem. *Solar Physics*, 234(1):41–77.
- Kohnert, R., Palo, S., and Li, X. (2011). Small Space Weather Research Mission Designed Fully by Students. *Space Weather*, 9(4):n/a–n/a.
- Krista, L. D. and Reinard, A. (2013). STUDY OF THE RECURRING DIMMING REGION DETECTED AT AR 11305 USING THE CORONAL DIMMING TRACKER (CoDiT). *The Astrophysical Journal*, 762(2):91.
- Labrosse, N. and Mcglinchey, K. (2012). Plasma diagnostic in eruptive prominences from SDO / AIA observations at 304 Å. *Astronomy & Astrophysics*, 537:A100.
- Landi, E., Del Zanna, G., Young, P. R., Dere, K. P., Mason, H. E., and Landini, M. (2006). CHIANTIAn Atomic Database for Emission Lines. VII. New Data for XRays and Other Improvements. *The Astrophysical Journal Supplement Series*, 162:261–280.
- Li, X., Palo, S., Kohnert, R., Blum, L., Gerhardt, D., Schiller, Q., and Califf, S. (2013a). Small Mission Accomplished by Students-Big Impact on Space Weather Research. *Space Weather*, 11(2):55–56.
- Li, X., Palo, S., Kohnert, R., Gerhardt, D., Blum, L., Schiller, Q., Turner, D., Tu, W., Sheiko, N., and Cooper, C. S. (2012). Colorado Student Space Weather Experiment: Differential Flux Measurements of Energetic Particles in a Highly Inclined Low Earth Orbit. In Summers, D., Mann, I. R., Baker, D. N., and Schulz, M., editors, *Dynamics of the Earth's Radiation Belts and Inner Magnetosphere*, Geophysical Monograph Series, pages 385–411, Washington, D. C. American Geophysical Union.

- Li, X., Schiller, Q., Blum, L., Califf, S., Zhao, H., Tu, W., Turner, D. L., Gerhardt, D., Palo, S., Kanekal, S., Baker, D. N., Fennell, J., Blake, J. B., Looper, M., Reeves, G. D., and Spence, H. (2013b). First results from CSSWE CubeSat: Characteristics of relativistic electrons in the near-Earth environment during the October 2012 magnetic storms. *Journal of Geophysical Research: Space Physics*, 118(10):6489–6499.
- Li, X., Selesnick, R. S., Baker, D. N., Jaynes, A. N., Kanekal, S. G., Schiller, Q., Blum, L., Fennell, J., and Blake, J. B. (2015). Upper limit on the inner radiation belt MeV electron intensity. *Journal of geophysical research. Space physics*, 120(2):1215–1228.
- Lin, R. P., Dennis, B. R., Hurford, G. J., Smith, D. M., Zehnder, A., Harvey, P. R., Curtis, D. W., Pankow, D., Turin, P., Bester, M., Csillaghy, A., Lewis, M., Madden, N., Beek, H. F., Appleby, M., Raudorf, T., McTiernan, J., Ramaty, R., Schmahl, E., Schwartz, R., Krucker, S., Abiad, R., Quinn, T., Berg, P., Hashii, M., Sterling, R., Jackson, R., Pratt, R., Campbell, R. D., Malone, D., Landis, D., Cork, C., Tolbert, A. K., Zarro, D. M., Snow, F., Thomsen, K., and Henneck, R. (2002). The Reuven Ramaty High-Energy Solar Spectroscopic Imager (RHESSI). *Solar Physics*, 210:3–32.
- Liu, W. and Ofman, L. (2014). Advances in Observing Various Coronal EUV Waves in the SDO Era and Their Seismological Applications (Invited Review). *Solar Physics*, 289(9):3233–3277.
- Mason, J. P., Woods, T. N., Caspi, A., Thompson, B. J., and Hock, R. A. (2014). MECHANISMS AND OBSERVATIONS OF CORONAL DIMMING FOR THE 2010 AUGUST 7 EVENT. *The Astrophysical Journal*, 789(1):61.
- Muhr, N., Veronig, A. M., Kienreich, I. W., and Temmer, M. (2011). Analysis of Characteristic Parameters of Large-Scale Coronal Waves Observed by the Solar-Terrestrial Relations Observatory/Extreme Ultraviolet Imager. *The Astrophysical Journal*, 89:89.
- Palo, S., Li, X., Gerhardt, D., Turner, D., Kohnert, R., Hoxie, V., and Batiste, S. (2010). Conducting Science with a CubeSat: The Colorado Student Space Weather Experiment.
- Parker, E. N. (1988). Nanoflares and the solar X-ray corona. *The Astrophysical Journal*, 330:474.
- Pearson, K. (1895). Note on Regression and Inheritance in the Case of Two Parents. *Proceedings of the Royal Society of London*, 58:240–242.
- Peterson, W. K., Stavros, E. N., Richards, P. G., Chamberlin, P. C., Woods, T. N., Bailey, S. M., and Solomon, S. C. (2009). Photoelectrons as a tool to evaluate spectral variations in solar EUV irradiance over solar cycle timescales. *Journal of Geophysical Research*, 114:A10304.
- Pohjolainen, S., Vilmer, N., Khan, J. I., and Hillaris, A. E. (2005). Early signatures of large-scale field line opening Multi-wavelength analysis of features connected with a halo CME event. *Astronomy & Astrophysics*, 434:329–341.
- Reinard, A. A. and Biesecker, D. A. (2008). Coronal Mass Ejection-Associated Coronal Dimmings. *The Astrophysical Journal*, 674:576–585.
- Reinard, A. A. and Biesecker, D. A. (2009). The Relationship Between Coronal Dimming and Coronal Mass Ejection Properties. *The Astrophysical Journal*, 705(1):914–919.

- Robbrecht, E. and Wang, Y.-M. (2010). The Temperature-Dependent Nature of Coronal Dimmings. *The Astrophysical Journal Letters*, 720:88–92.
- Rodgers, E. M., Bailey, S. M., Warren, H. P., Woods, T. N., and Eparvier, F. G. (2006). Soft X-ray irradiances during solar flares observed by TIMED-SEE. *Journal of Geophysical Research*, 111(A10):A10S13.
- Rompolt, . (1967). The H α Radiation Field in the Solar Corona for Moving Prominences. *Acta Astronomica*, 17.
- Schiller, Q., Gerhardt, D., Blum, L., Li, X., and Palo, S. (2014a). Design and scientific return of a miniaturized particle telescope onboard the Colorado Student Space Weather Experiment (CSSWE) CubeSat. In *2014 IEEE Aerospace Conference*, pages 1–14. IEEE.
- Schiller, Q., Li, X., Blum, L., Tu, W., Turner, D. L., and Blake, J. B. (2014b). A nonstorm time enhancement of relativistic electrons in the outer radiation belt. *Geophysical Research Letters*, 41(1):7–12.
- Schiller, Q. and Mahendrakumar, A. (2010). REPTile: A Miniaturized Detector for a CubeSat Mission to Measure Relativistic Particles in Near-Earth Space.
- Schlemm, C. E., Starr, R. D., Ho, G. C., Bechtold, K. E., Hamilton, S. A., Boldt, J. D., Boynton, W. V., Bradley, W., Fraeman, M. E., Gold, R. E., Goldsten, J. O., Hayes, J. R., Jaskulek, S. E., Rossano, E., Rumpf, R. A., Schaefer, E. D., Strohbehn, K., Shelton, R. G., Thompson, R. E., Trombka, J. I., and Williams, B. D. (2007). The X-Ray Spectrometer on the MESSENGER Spacecraft. *Space Science Reviews*, 131(1-4):393–415.
- Schrijver, C. J. and Higgins, P. A. (2015). A Statistical Study of Distant Consequences of Large Solar Energetic Events. *Solar Physics*, 290(10):2943–2950.
- Solomon, S. C., Bailey, S. M., and Woods, T. N. (2001). Effect of solar soft X-rays on the lower ionosphere. *Geophysical Research Letters*, 28(11):2149–2152.
- Sterling, A. C. and Hudson, H. S. (1997). YOHKOH SXT OBSERVATIONS OF X-RAY DIMMING ASSOCIATED WITH A HALO CORONAL MASS EJECTION. *The Astrophysical Journal*, 491:L55–L58.
- Swings, P. (1941). Complex Structure of Cometary bands Tentatively Ascribed to the Contour of the Solar Spectrum. *Lick Observatory Bulletin*, 508.
- Thompson, B. J., Cliver, E. W., Nitta, N. V., Delannée, C., and Delaboudiniere, J. P. (2000). Coronal Dimmings and Energetic CMEs in April-May 1998. *Geophysical Research Letters*, 27(10):1431–1434.
- Tian, H., McIntosh, S. W., Xia, L., He, J., and Wang, X. (2012). What Can We Learn About Solar Coronal Mass Ejections, Coronal Dimmings, and Extreme-Ultraviolet Jets Through Spectroscopic Observations? *The Astrophysical Journal*, 748(2):106.
- Vourlidas, A., Howard, R. A., Esfandiari, E., Patsourakos, S., Yashiro, S., and Michalek, G. (2010). Comprehensive Analysis of Coronal Mass Ejection Mass and Energy Properties Over a Full Solar Cycle. *The Astrophysical Journal*, 722:1522–1538.

- Vourlidas, A., Howard, R. A., Esfandiari, E., Patsourakos, S., Yashiro, S., and Michalek, G. (2011). ERRATUM : COMPREHENSIVE ANALYSIS OF CORONAL MASS EJECTION MASS AND ENERGY PROPERTIES OVER A FULL SOLAR CYCLE (2010 , ApJ , 722 , 1522). 59:2010–2012.
- Vourlidas, A., Subramanian, P., Dere, K. P., and Howard, R. A. (2000). LargeAngle Spectrometric Coronagraph Measurements of the Energetics of Coronal Mass Ejections. *The Astrophysical Journal*, 534(1):456–467.
- Woods, T. N. and Chamberlin, P. C. (2009). Comparison of solar soft X-ray irradiance from broadband photometers to a high spectral resolution rocket observation. *Advances in Space Research*, 43:349–354.
- Woods, T. N., Chamberlin, P. C., Peterson, W. K., Meier, R. R., Richards, P. G., Strickland, D. J., Lu, G., Qian, L., Solomon, S. C., Iijima, B. A., Mannucci, A. J., and Tsurutani, B. T. (2008). XUV Photometer System (XPS): Improved Solar Irradiance Algorithm Using CHIANTI Spectral Models. *Solar Physics*, 250(2):235–267.
- Woods, T. N., Eparvier, F. G., Bailey, S. M., Chamberlin, P. C., Lean, J., Rottman, G. J., Solomon, S. C., Tobiska, W. K., and Woodraska, D. L. (2005a). Solar EUV Experiment (SEE): Mission overview and first results. *Journal of Geophysical Research*, 110:A01312.
- Woods, T. N., Hock, R. A., Eparvier, F. G., Jones, A. R., Chamberlin, P. C., Klimchuk, J. A., Didkovsky, L., Judge, D., Mariska, J. T., Warren, H. P., Schrijver, C. J., Webb, D. F., Bailey, S. M., and Tobiska, W. K. (2011). New Solar Extreme-Ultraviolet irradiance Observations During Flares. *The Astrophysical Journal*, 739:59.
- Woods, T. N., Rottman, G., and Vest, R. (2005b). XUV Photometer System (XPS): Overview and Calibrations. *Solar Physics*, 230(1-2):345–374.
- Zhukov, A. N. and Auchère, F. (2004). On the nature of EIT waves, EUV dimmings and their link to CMEs. *Astronomy & Astrophysics*, 427:705–716.